

# Design and evaluation of an ultra-slim objective for *in-vivo* deep optical biopsy

Sara M. Landau,<sup>1\*</sup> Chen Liang,<sup>2</sup> Robert T. Kester,<sup>3</sup> Tomasz S. Tkaczyk,<sup>3</sup> and Michael R. Descour<sup>1</sup>

<sup>1</sup>University of Arizona, College of Optical Sciences, 1630 E. University Blvd., Tucson, AZ, 85721, USA

<sup>2</sup>DMetrix, Inc., 1141 West Grant Rd, Suite 100, Tucson, AZ, 85705, USA

<sup>3</sup>Rice University, Department of Bioengineering, MS 142, 6100 Main St., Houston, TX, 77005, USA  
\*slandau@optics.arizona.edu

**Abstract:** An estimated 1.6 million breast biopsies are performed in the US each year. In order to provide real-time, *in-vivo* imaging with sub-cellular resolution for optical biopsies, we have designed an ultra-slim objective to fit inside the 1-mm-diameter hypodermic needles currently used for breast biopsies to image tissue stained by the fluorescent probe proflavine. To ensure high-quality imaging performance, experimental tests were performed to characterize fiber bundle's light-coupling efficiency and simulations were performed to evaluate the impact of candidate lens materials' autofluorescence. A prototype of NA = 0.4, 250- $\mu\text{m}$  field of view, ultra-slim objective optics was built and tested, yielding diffraction-limited performance and estimated resolution of 0.9  $\mu\text{m}$ . When used in conjunction with a commercial coherent fiber bundle to relay the image formed by the objective, the measured resolution was 2.5  $\mu\text{m}$ .

©2010 Optical Society of America

**OCIS codes:** (220.3620) Lens system design; (350.3950) Micro-optics; (170.2150) Endoscopic imaging.

---

## References and links

1. M. Silverstein, "Where's the outrage?" *J. Am. Coll. Surg.* **208**(1), 78–79 (2009).
2. V. Dubaj, A. Mazzolini, A. Wood, and M. Harris, "Optic fibre bundle contact imaging probe employing a laser scanning confocal microscope," *J. Microsc.* **207**(2), 108–117 (2002).
3. T. J. Muldoon, M. C. Pierce, D. L. Nida, M. D. Williams, A. Gillenwater, and R. Richards-Kortum, "Subcellular-resolution molecular imaging within living tissue by fiber microendoscopy," *Opt. Express* **15**(25), 16413–16423 (2007).
4. W. Zhong, J. P. Celli, I. Rizvi, Z. Mai, B. Q. Spring, S. H. Yun, and T. Hasan, "In vivo high-resolution fluorescence microendoscopy for ovarian cancer detection and treatment monitoring," *Br. J. Cancer* **101**(12), 2015–2022 (2009).
5. D. Toomre, and J. B. Pawley, "Disk-scanning confocal microscopy," in *Handbook of biological confocal microscopy*, J. B. Pawley, ed. (Springer, New York, 2006), pp. xxviii, 985 p.
6. R. Richards-Kortum, Department of Bioengineering, Rice University, MS 142, 6100 Main St., Houston, TX, 77005, USA (personal communication, 2010).
7. PENTAX Medical Company, Montvale, NJ 07645, <http://www.pentaxmedical.com/brochures/Confocal.pdf>.
8. Optiscan Pty. Ltd., Victoria, Australia, 3168 [http://www.optiscan.com/Products/FIVE1\\_Brochure.pdf](http://www.optiscan.com/Products/FIVE1_Brochure.pdf).
9. R. T. Kester, T. S. Tkaczyk, M. R. Descour, T. Christenson, and R. Richards-Kortum, "High numerical aperture microendoscope objective for a fiber confocal reflectance microscope," *Opt. Express* **15**(5), 2409–2420 (2007).
10. S. Santos, K. K. Chu, D. Lim, N. Bozinovic, T. N. Ford, C. Hourtoule, A. C. Bartoo, S. K. Singh, and J. Mertz, "Optically sectioned fluorescence endomicroscopy with hybrid-illumination imaging through a flexible fiber bundle," *J. Biomed. Opt.* **14**(3), 030502 (2009).
11. A. R. Rouse, A. Kano, J. A. Udovich, S. M. Kroto, and A. F. Gmitro, "Design and demonstration of a miniature catheter for a confocal microendoscope," *Appl. Opt.* **43**(31), 5763–5771 (2004).
12. P. Kim, M. Puoris'haag, D. Côté, C. P. Lin, and S. H. Yun, "In vivo confocal and multiphoton microendoscopy," *J. Biomed. Opt.* **13**(1), 010501 (2008).
13. S. Georghiou, "Interaction of acridine drugs with DNA and nucleotides," *Photochem. Photobiol.* **26**(1), 59–68 (1977).
14. A. F. Gmitro, and D. Aziz, "Confocal microscopy through a fiber-optic imaging bundle," *Opt. Lett.* **18**(8), 565–567 (1993).

15. "Normal anatomy of the breast," Yale University School of Medicine, [http://www.med.yale.edu/intmed/cardio/imaging/anatomy/breast\\_anatomy/index.html](http://www.med.yale.edu/intmed/cardio/imaging/anatomy/breast_anatomy/index.html).
16. M. D. Chidley, K. D. Carlson, R. R. Richards-Kortum, and M. R. Descour, "Design, assembly, and optical bench testing of a high-numerical-aperture miniature injection-molded objective for fiber-optic confocal reflectance microscopy," *Appl. Opt.* **45**(11), 2545–2554 (2006).
17. ZEMAX Development Corporation, Bellevue, WA 98004–8017, <http://www.zemax.com/>.
18. L. P. Zeon Chemicals, Louisville, KY 40211, <http://www.zeonchemicals.com/>
19. R. R. Shannon, *The Art and Science of Optical Design* (Cambridge University Press, 1997).
20. W. C. Sweatt, D. D. Gill, D. P. Adams, M. J. Vasile, and A. A. Claudet, "Diamond milling of micro-optics," *IEEE Aerosp. Electron. Syst. Mag.* **23**(1), 13–17 (2008).
21. R. T. Kester, T. Christenson, R. Richards-Kortum, and T. Tkaczyk, "High Performance Self Aligning Miniature Optical Systems for in vivo Diagnostics," (Optical Society of America, 2008)
22. B. Saleh, and M. Teich, *Fundamentals of Photonics* (Wiley-Interscience, 1991).
23. ISO 12233:2000(E), *Photography - electronic still picture cameras - Resolution measurements* (2000).
24. A. P. Tzannes, and J. M. Mooney, "Measurement of the modulation transfer-function of infrared cameras," *Opt. Eng.* **34**(6), 1808–1817 (1995).
25. J. D. Gaskill, *Linear Systems, Fourier Transforms, and Optics* (John Wiley and Sons, 1978).
26. E. Hecht, *Optics, Fourth Edition* (Addison Wesley, 2002).
27. C. Liang, K.-B. Sung, R. R. Richards-Kortum, and M. R. Descour, "Design of a high-numerical-aperture miniature microscope objective for an endoscopic fiber confocal reflectance microscope," *Appl. Opt.* **41**(22), 4603–4610 (2002).

## 1. Introduction

An estimated 1.6 million breast biopsies are performed in the US each year [1]. The current clinical procedure is to use surgical biopsy, core needle biopsy or fine needle aspiration to acquire pathologic specimens in areas of tissue that have been classified as abnormal using PET or MRI. The cells are then fixed to a microscope slide, stained, and examined by a pathologist. While this method does yield information about the tumor architecture and cell morphology, it only samples small sections of the tumor. Such sampling can be problematic if the tumor is large and heterogeneous. The tissue acquired may not contain enough viable cells or may not contain cells from the malignant section of the tumor thus complicating the diagnosis by potentially requiring additional biopsies or resulting in misdiagnosis. Also, this process of cell extraction and staining does not allow for real-time diagnosis.

Optical imaging modalities are capable of real-time imaging and *in-vivo* imaging with sub-cellular resolution. Examples include optical coherence tomography (OCT) and confocal microscopy. However, the maximum penetration depth is less than 3 mm for optical imaging modalities. One way to achieve the penetration-depth capabilities of PET in combination with sub-cellular resolution is through the use of an optical biopsy approach.

To be consistent with the current tissue-removal biopsy techniques, an optical-biopsy system would need to produce images of cell morphology for the pathologist to examine and have a similar outer diameter as the needles currently used for needle biopsies (0.6–3 mm). For this article, we limit our review to a slightly expanded ensemble of optical systems whose outer diameters (ODs) are 5 mm or less and to those optical systems intended for linear fluorescence microscopy. Within these constraints, there exist two types of microendoscopes. The first type is the fiber microendoscope where a coherent fiber bundle is pressed in direct contact with the tissue to relay an image of the tissue out of the body. The second type utilizes optical elements to focus the light before the image is transferred out of the body. The advantages of fiber microendoscope systems derive from the simplicity of their design and the small diameter of the fiber bundles used, typically 0.6 mm to 0.8 mm OD [2,3]. However, the resolution of the fiber microendoscope systems is determined by the core spacing in the fiber bundle. The current minimum lateral resolution for these systems is approximately 4.4  $\mu\text{m}$  for a fiber bundle with a numerical aperture (NA) of 0.35 [3]. In comparison, the system presented in this paper has a 0.4 NA but can resolve details down to 0.9  $\mu\text{m}$ . Image processing can be used to improve the pixilated appearance of images taken with a fiber microendoscope, although processing does not improve the actual resolution [4]. Additionally, lens-based microendoscopes provide a small depth of field, which aids in

optical sectioning. For example, the system we have designed has an estimated axial resolution of  $6\ \mu\text{m}$  [5], which is thinner than a layer of cells. In contrast, a lensless, fiber-bundle-based system has a much larger depth of field, typically larger than a single layer of cells [2,6].

The second type of microendoscope can be divided further into two categories defined by their ODs, specifically  $\text{OD} < 1\ \text{mm}$  and  $1\ \text{mm} \leq \text{OD} < 5\ \text{mm}$ . In the larger OD category, several systems have been documented in the literature or are commercially available [7–11], including systems with a minimum lateral resolution to  $0.7\ \mu\text{m}$  [7,8]. To the best of our knowledge, there is currently only one system designed for linear fluorescence microscopy with an OD of  $1\ \text{mm}$  [12]. However, the objective of this system, whose lateral resolution is approximately  $1.5\ \mu\text{m}$ , utilizes gradient-index lenses, which cannot be achromatized and inherently suffer from spatial and chromatic aberrations.

To add to this category of microendoscopes, we have designed an all-plastic, ultra-slim objective to fit inside the 1-mm inner diameter of hypodermic needles (18 gauge) currently used for breast biopsies. The objective is mounted inside the distal end of the needle as shown in Fig. 1 along with a coherent fiber bundle to relay the image of the tissue out of the needle. The needle would be then inserted into the breast, and the distal end of the objective pressed in contact with the tissue stained by the fluorescent probe proflavine [13], thus reducing image motion [3]. In order to produce images usable to a pathologist, the system would be used in a larger confocal microscope setup. Here a single fiber or a small group of fibers could be illuminated and imaged in order to reject out-of-focus light and provide the optical sectioning needed to image only a thin slice of tissue within the larger tissue volume [14]. Additionally, we envision that as the needle proceeds into the tissue, the objective relays sub-cellular images of the tissue architecture and morphology in real-time. Once the objective reaches the tumor, an immediate assessment of the tumor can be made by the pathologist who could probe multiple locations in the tumor to increase the accuracy of the diagnosis. While the emphasis of this design was to facilitate breast cancer diagnosis, the ultra-slim objective could be used in other parts of the body where needle biopsies are a common diagnostic method, such as the lung, thyroid, parathyroid, and pancreas.

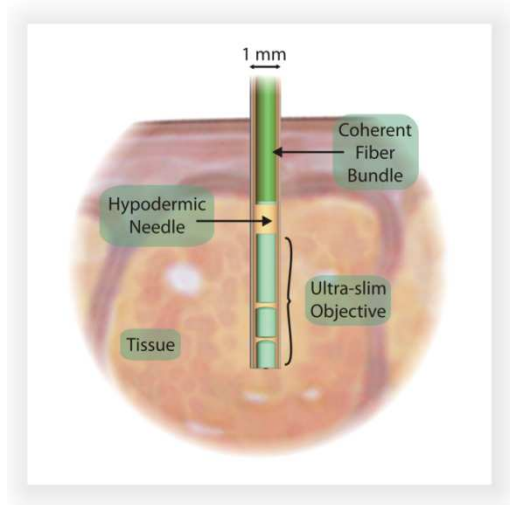


Fig. 1. Illustration of the ultra-slim objective and coherent fiber bundle in the hypodermic needle within the tissue [15].

In this paper we describe the design parameters of the ultra-slim objective, as well as the manufacturing and assembly methods that are required to produce an objective with high image quality. As the manufacturing and assembly of miniature optical systems is a costly

and time consuming process [9,16], careful planning is required to produce a working, practical system. To that end, this paper also describes conventional lens imaging limitations and tradeoffs found as the size of the objective decreases into the sub-millimeter range, as well as experimental measurements to estimate light-coupling limitations and the impact of autofluorescence of candidate lens materials.

## 2. Ultra-slim objective design parameters

The general design specifications based on the intended use of the ultra-slim objective can be found in Table 1. First, the field of view (FOV) needs to sample an adequate number of cells. For this application the FOV diameter is 250  $\mu\text{m}$ . Second, for mounting the lens system within a 1 mm tube as discussed in Section 3, the clear apertures of the lenses and the proximal face of the coherent fiber bundle where the image plane is located must be less than 0.8 mm in diameter, which leads to a transverse magnification of  $-3.2$  for this FOV. Additionally, for adequate spatial resolution, the object-space numerical aperture (NA) of the system is 0.4. This translates into an image-space NA of 0.125. The fibers in the bundle have an NA of 0.35, so stray light has to be considered when finalizing the design of the ultra-slim objective housing. The working distance of the objective is approximately 10  $\mu\text{m}$  to ensure that the object surface in contact with the tissue is outside the first element of the objective once the objective has been fabricated and assembled. Also, the objective is optimized for a wavelength of 508 nm, the peak emission wavelength of proflavine and an excitation wavelength of 470 nm.

**Table 1. General Design Specifications**

Object Space NA	0.4
Image-space NA	0.125
Field of View (FOV)	250 $\mu\text{m}$
Clear Aperture	0.8 mm
Magnification	$-3.2$
Working Distance	10 $\mu\text{m}$
Wavelength	508 nm
Object-space Telecentric	Yes

The design for the ultra-slim objective was performed using ZEMAX lens design software [17] and consists of three optical elements made of Zeonex (E48R) [18], as shown in Fig. 2. A coverslip placed over the face of the coherent fiber bundle reduces back reflections from the face of the coherent fiber bundle. Both the first and the last surface of the lens system are flat, which simplifies the fabrication and mounting of the elements. Also, the four surfaces that contribute to the power of the system are conics [see Table 2 for prescription], which allows more flexibility in the optical design by aiding in the correction of aberrations while keeping the number of parameters low to aid the lens-optimization process. Additionally, the objective focuses to a slightly curved object surface that has a sag of 9.7  $\mu\text{m}$ , as shown in Fig. 2(b). Because the tissue being imaged is a 3D volume of cells, curving the object plane does not overly distort the image and helps with the correction of aberrations.

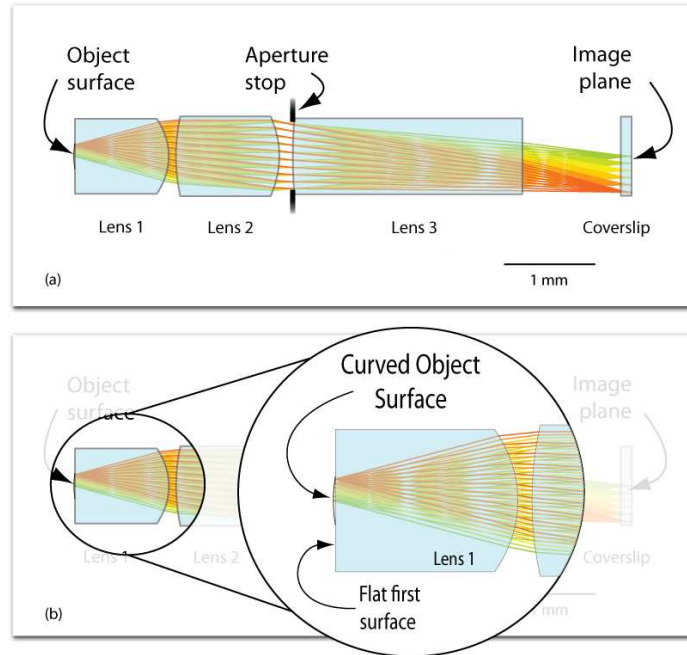


Fig. 2. (a) Design layout for ultra-slim objective, (b) Enlargement illustrating the curvature of the object surface.

Table 2. Lens System Prescription for design in Fig. 2.

Surface	Comment	Radius (mm)	Thickness (mm)	Glass	Clear Aperture (mm)	Conic
Object Surface	Tissue	0.8	0.014	Saline	0.25	-
1	Lens 1	Plano Surface	1.04	E48R	0.25	-
2		-0.69	0.08		0.75	-0.34
3	Lens 2	1.94	1.15	E48R	0.8	-4.64
4		-0.99	0.15		0.8	-1.21
Aperture Stop	Lens 3	5.57	2.55	E48R	0.72	36.65
6		Plano Surface	1.09		0.77	-
7	Coverslip	Plano Surface	0.12	BK7	0.8	-
Image Plane	Fiber Bundle	Plano Surface	0		0.8	-

The predicted image performance can be seen in Fig. 3, which shows the combined spot diagram and point spread function (PSF) for three field positions. The white gradient in the center represents a top view of the PSF where the white ring is the Airy disk located at the first zero of the PSF, and the red dots are the spot diagram. Because all of the spots lie within the Airy disk, the design is diffraction limited. Calculations in ZEMAX evaluate the Strehl ratio to be greater than 0.8, i.e., the accepted Strehl ratio for a well corrected system [19].

Additionally, ZEMAX was used to estimate the performance of the ultra-slim objective when used to image the polychromatic emission spectrum of proflavine. The wavelengths of the emission spectrum were weighted by the intensity relative to the peak emission, and added to the ZEMAX design shown in Fig. 2(a). To maintain a Strehl ratio of 0.8, a spectral

filter was used to limit the emission spectrum to the range of 486 nm to 546 nm, which results in 66% of the emitted light reaching the image plane.

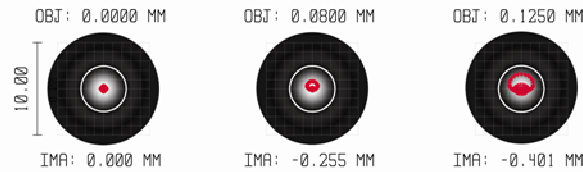


Fig. 3. The performance of the objective design, showing both the PSF as the white gradient and the diffraction-limited spot diagram in red at three field positions (on-axis, 80  $\mu\text{m}$  off axis, and 125  $\mu\text{m}$  off-axis, i.e., at the edge of the useful field of view).

### 3. Manufacturing, assembly, and tolerancing of prototype system

#### 3.1 Manufacturing and assembly

Modern manufacturing methods of the lenses and novel mounting solutions are both required to produce an objective with lens diameters less than 1 mm. Specifically, since good image quality requires small form error and low surface roughness, one effective method of fabricating spherical and aspheric lenses with adequately high quality is single point diamond turning (SPDT). Previous in-house SPDT manufacturing has yielded lenses with a peak-to-valley form error of 1/10th of a wave and average roughness ( $R_a$ ) of 18 nm. Alternatively, diamond milling tools with shaped tips can also be used to make high precision lenses, however, fabrication of aspheric surfaces with such tools is at a very early stage of development [20].

Mounting of lenses on the 1-mm scale may be accomplished ultimately with miniature, self-aligning holders fabricated using the LIGA process [21]. LIGA is a German acronym for X-ray lithography, electroplating, and molding, and is a micro-lithography process that can produce micro-optical mounts with sub-micron precision. However, in order to expedite the experimental evaluation of the optical design itself [see Fig. 2(a)], the prototype lenses as described in Section 6 were diamond turned on larger-diameter blanks and stacked using precision ball bearings.

#### 3.2 Tolerance analysis

To ensure that a successful prototype would be fabricated, tolerance analysis was performed using the criterion for the maximum allowable error of 0.07 waves of *rms* wavefront error (WFE), which corresponds to the Strehl ratio of 0.8. For comparison, the nominal WFE of the design was 0.012 waves. Using ZEMAX to perform the analysis on a symmetric cross of  $x$  and  $y$  field positions, the tolerances in Table 4 were established. Additionally, Monte Carlo analysis was performed using ZEMAX to generate 500 perturbed optical systems. The mean WFE for the trials was 0.0536 waves, and over 80% of the trials had a WFE less than 0.07 waves. Using standard definitions of tolerance levels [19], the majority of the tolerances in Table 3 fall under either *commercial* or *precision* tolerance requirements with only the decenters on Surface 2, Lens 1, and Lens 2 requiring *high-precision* manufacturing.

**Table 3. Fabrication and Optomechanical Tolerances**

		Lens 1		Lens 2		Lens 3	
		Nominal (mm)	Tolerance (mm)	Nominal (mm)	Tolerance (mm)	Nominal (mm)	Tolerance (mm)
Surface 1	Radius	Plano	-	1.944	0.019	5.566	0.055
	Decenter	0	0.01	0	0.01	0	0.01
	Tilt	0	0.01	0	0.0038	0	0.01
Surface 2	Radius	-0.694	0.007	-0.994	0.007	Plano	-
	Decenter	0	0.008	0	0.007	0	0.01
	Tilt	0	0.01	0	0.0035	0	0.01
Element	Thickness	1.04	0.008	1.147	0.016	2.547	0.016
	Airspace to Next Lens	0.08	0.016	0.15	0.016	Compensator	-

The prototype reported here was fabricated at DMetrix, Inc., which was able to fabricate miniature optics to the tighter tolerances listed in Table 4. With the exception of the tilt tolerances, all of the tolerances in Table 5 are *high precision* [19]. When these tolerances were used in the ZEMAX tolerance analysis, a WFE of 0.04 waves was predicted. The same Monte Carlo analysis was performed with the tightened tolerances. The mean WFE for the second set of trials was 0.0254 waves, and over 98% of the trials had a WFE less than 0.07 waves.

**Table 4. Fabrication capabilities used to make prototype objective.**

Parameter	Tolerance
Radius (μm)	4
Decenter (μm)	5
Thickness (μm)	5
Tilt (°)	0.12

#### 4. Design considerations for sub-millimeter objectives

As applications for smaller objectives multiply, it is important to look at the limitations of conventional lens imaging at the millimeter size scale. One such limitation is the tradeoff between the transverse magnification and the FOV for the objective. In general, it is preferred to have a large magnification to see cellular and sub-cellular scale features. However, as the magnification increases, the FOV decreases so that only a few cells are imaged and the usefulness of the objective for cancer detection is diminished.

A system that is image-space telecentric is also preferred so that translation of a detector or fiber bundle at the image plane does not result in a magnification change. In the case of the fiber bundle, image-space telecentricity also means that light is focused on each fiber in the bundle over the same part of the fiber’s acceptance numerical aperture. However, image-space telecentricity is difficult to achieve in very small objective systems. In order for the objective to be both image-space telecentric and unvignetted, the clear-aperture diameter of the last element of the objective must be greater than the image-plane diameter. Therefore, for a given field of view, the image-space telecentricity requirement limits the maximum transverse magnification and results in underfilling the available image area.

In order to fill the largest image-plane area within the inner-diameter constraint of the biopsy needle, we made a compromise in the design of the ultra-slim objective and relaxed

the constraint on the image-space telecentricity. This allowed the light in the off-axis ray bundles incident on the image plane to have a non-zero principal ray angle with respect to the optical axis as illustrated in Fig. 4(a) and can be seen in the optical layout in Fig. 2(a). However, one tradeoff associated with allowing a non-zero principal ray angle is that as the angle of incidence of the principal ray increases, the distortion in the image becomes more difficult to compensate for and the image-quality decreases. An additional tradeoff associated with allowing a non-zero principal ray angle is that if the objective couples light into a coherent fiber bundle, or a scanned single optical fiber, the light-coupling efficiency decreases. There are two major reasons for this decrease. First, the cone of light exiting the objective is misaligned with the acceptance cone of the fibers [see Fig. 4(b)] so that light at the edge of the incident ray bundle is not coupled into the fiber.

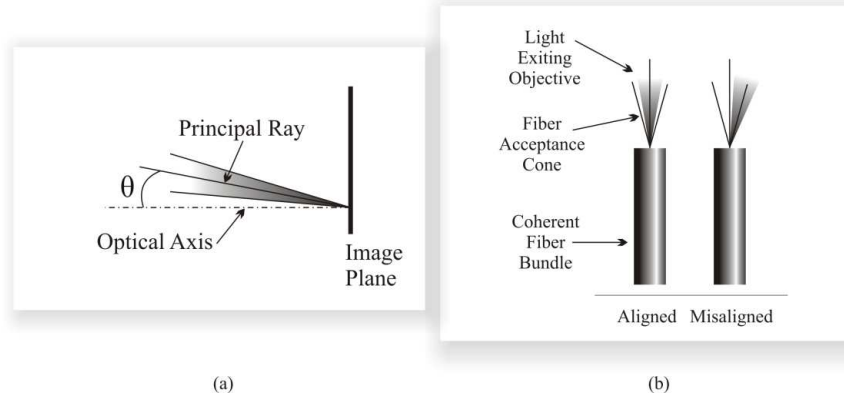


Fig. 4. (a) Principal Ray Angle incident on Image Plane, (b) Diagram of light exit objective alignment with fiber acceptance cone.

Second, for a given fiber there exists a transition angle,  $\theta_t$ , dependent on the wavelength, fiber core diameter, and fiber NA [22]. Rays entering the fiber below  $\theta_t$  excite the zeroth order mode, and rays with an incident angle greater than  $\theta_t$  excite first order mode. For a ray bundle that straddles  $\theta_t$  [see Fig. 5(a)], a mixture of the two modes is excited, and the light exiting the fiber has a non-uniform intensity [see Fig. 5(b)]. Additionally, more light leaks into the cladding for light rays with incident angles greater than  $\theta_t$ , which also effectively decreases the coupling efficiency.

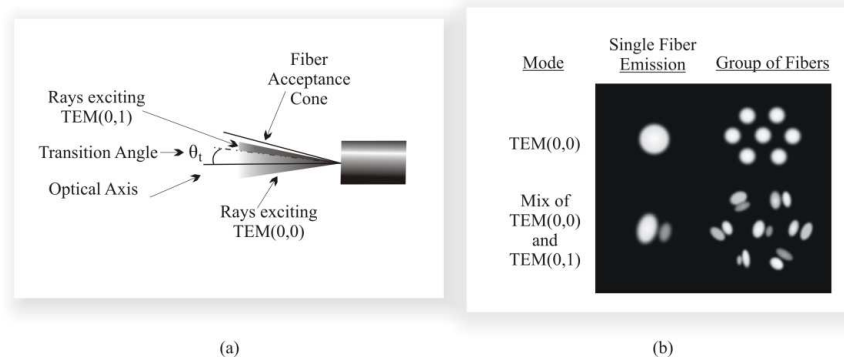


Fig. 5. Diagrams illustrating  $\theta_t$  and its effect on coupling. TEM(0,0) and TEM(0,1) stand for transverse electromagnetic wave zeroth order and first order mode, respectively. (a) Illustration of a ray bundle intersected by the transition angle, (b) Diagram of fiber emission depending on the mode of light.

However, the reduction in fiber coupling efficiency resulting from a non-zero principal-ray angle is less than the loss of light transmission if the optical system were telecentric in image space but vignetted at the outer parts of the FOV. To measure the fiber coupling efficiency with increasing principal-ray angle, we performed the experiment detailed in Section 5.1. To evaluate light transmission of a doubly telecentric optical system constrained by the clear-aperture requirement of the design specifications in Table 1, the design shown in Fig. 2(a) was redesigned to be doubly telecentric. The redesign was based on holding the prescription constant up to the aperture stop so that the front of the doubly telecentric design from the object surface through the second lens was identical and then allowing the surface radii, conic constants, and thickness of Lens 3, as well as the distance to the coverslip, to vary. A circular aperture was modeled after the second surface of Lens 3 to enforce the required clear aperture of the ultra-slim objective.

The blue line in Fig. 6 shows the effect of the vignetting caused by the aperture. For the doubly telecentric vignetted optical-design case, all of the light collected from the object is incident on the image plane out to a radial object distance of 80  $\mu\text{m}$ . However, from 80  $\mu\text{m}$  to edge of the field at 125  $\mu\text{m}$ , the light transmission efficiency falls below 40% due to the vignetting. Additionally, in this region the numerical aperture of the incident light is reduced as well, causing a gradual increase in the width of the point spread function towards the edge of the field. For comparison, the red line in Fig. 6 shows the reduction of fiber coupling efficiency in the design of Fig. 2(a) as the principal ray angle increases across the radial extent of the FOV. While the reduction in coupling efficiency begins immediately off axis, the reduction is gradual and, more importantly, falls to only 77% at the edge of the FOV. Compared to the vignetted design, almost twice as much light reaches the image plane at the FOV edge. Furthermore, the image quality can be expected to be higher and more uniform because the numerical aperture does not vary across the field as it does in the vignetted case.

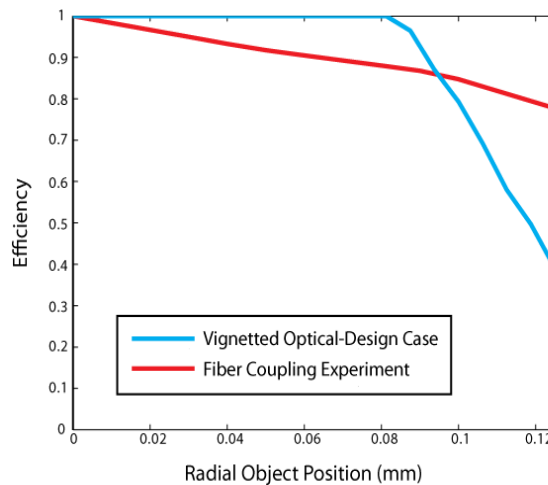


Fig. 6. Comparison between the efficiency of the light incident on the image plane of the doubly telecentric vignetted optical-design case and the relative coupling efficiency results of the fiber coupling experiment.

## 5. Experimental verification

### 5.1 Fiber coupling efficiency

Because the light level for fluorescent imaging is typically low, an experimental determination of the light-coupling efficiency with respect to increasing principal ray angle, and thus an important design constraint, was critical. The experimental setup was designed to

simulate the ultra-slim objective coupling efficiency by using the same coherent fiber bundle. For further consistency, the NA of the objective focusing the light onto the fiber bundle is the same as the image-space NA of the ultra-slim objective. Although this configuration was specific to our design, the experimental setup could be readily modified to test other fiber bundles, wavelengths, or NAs. The setup used [see Fig. 7] consisted of a commercial objective focusing a collimated, spatially filtered laser beam on to the proximal face of the fiber bundle, where the focusing objective is mounted on a computer-controlled,  $xy$  stages. The distal end of the bundle was imaged onto a camera. Additionally, a beam splitter was placed after the laser to direct a portion of the light to the radiometer head to monitor and record the fluctuations of the laser for later calibration. The specifications of the major components of the fiber coupling experimental set-up can be found in Table 5.

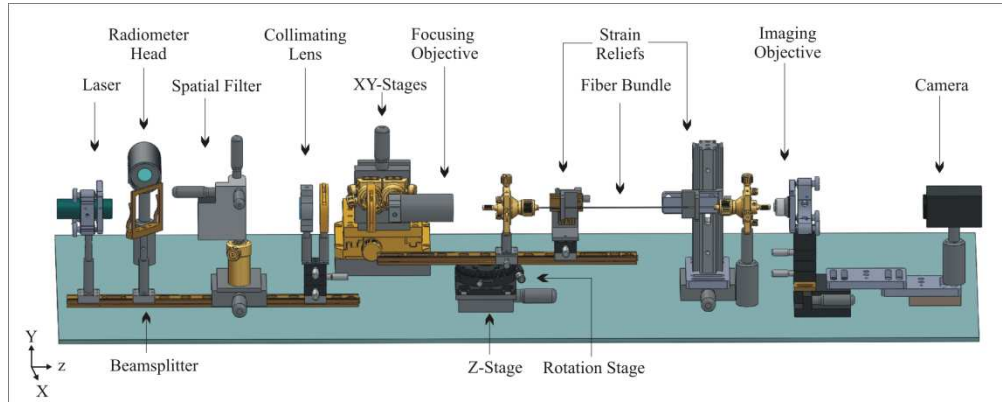


Fig. 7. Experimental setup for measurement of light-coupling efficiency into a coherent fiber bundle as a function of principal ray angle of incidence.

**Table 5. Major Components used in Fiber Coupling Experiment**

Manufacturer	Component
Edmund Optics	Infinity-Corrected Long Working Distance Objective, Plano Apochromat
JDS Uniphase	Laser HeNe, 635 nm
Lumenera Scientific	Infinity1 Camera
New Focus	Stages 9064 X-travel stage 1" Picomotor™ Actuator and controller
Newport	ESP 300 Motion Controller and stage Spatial Filter, Model 900
Sumitomo Electric	30,000 Element Coherent Optical Fiber, 0.8 mm diameter
Thorlabs	High Precision Rotation Mount
UDT Instruments	S370 Radiometer

The measurement procedure is as follows. Starting with the fiber face normal to the optical axis, a LabView script orchestrates the movement of the  $xy$  stages. In order to overcome environmental instabilities, a semi-recursive script was written to align the focused spot of focusing objective to a single fiber. The script development began by defining a metric to evaluate how well the light was focused onto a single fiber based on the image collected by the camera of the distal end of the fiber bundle. In this case, the metric used was the ratio of the intensity exiting the fiber of interest to the intensity of the neighboring fibers. The first step of the experiment was to align the focus manually with the aid of the computer-controlled stages. Then the focused spot was scanned in the  $y$ -direction, saving the image of the distal end of the fiber and evaluating the metric at each step. The script directed the  $y$ -stage to return to the position of best alignment, and the process was repeated for the  $z$ -

direction. In the  $x$ -direction, the  $xy$ -stages stepped in a small grid to collect images around the best alignment spot found in the previous two steps. After all the images have been taken, MATLAB script selected the set of images whose metric was above a user-defined threshold. For each image in the set MATLAB computed the intensity of the fiber of interest, and then averaged the intensity of the fiber from the set of images along with the standard deviation of the individual fiber intensities in the set of images. This procedure was performed for three randomly selected fibers at six different angles.

The results for the individual fibers average intensity relative to the on-axis measurement can be seen in Fig. 8(a), where the error bars are the standard deviation of the averaged set of images. To find a cut-off angle to use as a design constraint, the relative coupling efficiency at each angle for the three fibers was averaged. Using the results in Fig. 8(b), to couple more than 70% of light from the objective into a fiber, the principal ray angle must be constrained to less than  $6^\circ$ . This constraint was included in the design, and the largest principal ray angle incident on the fiber in the ultra-slim objective design was  $5.2^\circ$ .

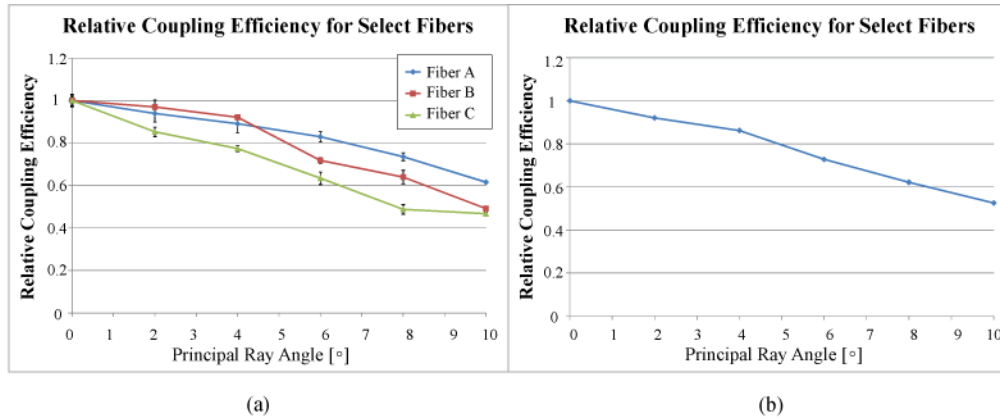


Fig. 8. Experimental fiber coupling efficiency data at six different angles. Note the connecting lines represent a decreasing trend and not measurements. (a) Experimental data showing the relationship between the intensity relative to on-axis and the principal ray angle for three randomly selected fibers, (b) The average of the relative coupling efficiency for the three fibers.

### 5.2 Autofluorescence of candidate lens materials

We measured the relative autofluorescence of candidate lens materials to verify that the amount of light excited in the lens material itself is low in comparison to a typical fluorescent emission, when coupled into a fiber at the image plane.

First, three optical-grade plastics commonly used for diamond turning and injection molding, i.e., Zeonex E48R, PMMA, and polystyrene were measured in a spectrofluorometer. The solid materials were shaped to the same dimensions as a standard cuvette. Second, data from these measurements were used in non-sequential ray tracing model to determine how much light would reach an optical fiber at the image plane of our optical design. For reference, we also tested a 1 nM solution of fluorescein.

The spectral emission measurements were taken with the FluoroLog<sup>®</sup>-3 spectrofluorometer (HORIBA Scientific), which produces a matrix of emission spectra from 270 to 720 nm for excitation wavelengths from 250 to 600 nm. For this analysis, we used emission spectra of each tested material obtained with 470 nm excitation light.

In order to determine how much light would reach an optical fiber at the image plane, we used non-sequential ray tracing in two separate configurations. In the first configuration, autofluorescent emission of the three lenses' volumes was modeled by bulk scattering in ZEMAX [17]. The bulk scattering model allowed us to simulate the absorption of 470 nm

excitation light within each lens and emission at 510 nm from each lens. In the second configuration, a fluorescent “object” volume was placed in front of the first lens surface and bulk scattering was turned off within each lens volume. The fluorescent object volume had the same diameter as the optical system (0.8 mm) and a thickness of 150  $\mu\text{m}$  to act like a thick section of tissue. The fluorescent object volume was modeled as filled with a 1 nM fluorescein solution. In both configurations, 470 nm light was emitted from a single on-axis fiber and a beam splitter was used to redirect the 510 nm emitted light into a detector with the specifications of a single on-axis fiber.

The bulk scattering analysis requires the estimation of a mean free path [17] for each modeled medium. Given the relative emissions at 510 nm from the 1 nM fluorescein solution and the lens materials, we estimated the MFP for each by modeling the cuvette in the spectrofluorometer with non-sequential ray tracing and bulk scattering. In the case of the 1 nM fluorescein solution, we set the ray-tracing MFP at 0.434 mm. Note that this value is much smaller than the  $2.7 \times 10^4$  mm MFP calculated from the optical cross-section per molecule and number of molecules per unit volume at 470 nm. The fluorescein ray-tracing MFP was selected so that we could model the solution with a reasonable number of rays traced (e.g.,  $10^6$ ). The ray-tracing MFPs for the lens materials were then established by finding the MFP at which the number of detected rays relative to the number of rays for fluorescein equaled the corresponding ratio of signals measured with the spectrofluorometer. Following this method, we estimated the ray-tracing MFP for Zeonex E48R to be 70.5 mm.

Four billion rays were traced in both of the bulk-scattering system simulations. In the case of Zeonex E48R, which had the highest autofluorescence of all the materials tested, the signal at the collector fiber from the fluorescing “object” volume was 28 times higher than the background signal due the autofluorescence of the lenses. Note that the 1 nM concentration corresponds to an average of only 3 fluorophore molecules in each  $5 \mu\text{m}^3$  voxel.

## 6. Prototype fabrication

The model cross-section can be seen in Fig. 9(a). The surfaces of each lens, highlighted in green, were single point diamond turned into the center of a one inch disc of Zeonex E48R, where the flat first and last surfaces were recessed slightly to prevent scratching. Then V-groove rings, concentric with the optical axis of the lens, were cut into the surrounding plastic to act as alignment features for mounting. Last, the discs were stacked in a circular holder by placing precision ball bearings into the V-grooves as shown in Fig. 9(a). The actual prototype can be seen in the holder as part of the test set-up [see Fig. 9(b)].

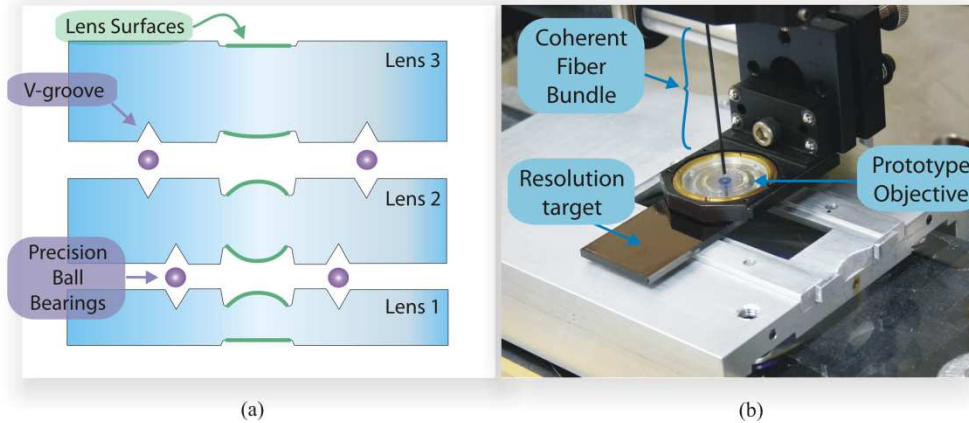


Fig. 9. (a) Schematic of the cross section of the prototype plates and the precision ball bearings, not to scale, (b) Photograph of the fabricated prototype plates stacked in a brass basket used in the test set-up.

## 7. Imaging performance

The ultra-slim objective was evaluated both qualitatively and quantitatively with fabricated resolution targets. The quantitative evaluation was based on tests which measure the point-spread function (PSF) and the modulation transfer function (MTF) at a position within the objective's FOV [16,23,24].

### 7.1 Qualitative imaging performance

The fabricated target consisted of several regions containing different gratings and features was used as an object for testing in the setup of Fig. 10. For this test three regions were used: a region containing small US Air Force Resolution target features and two regions containing gratings with periods of 25  $\mu\text{m}$  and 2  $\mu\text{m}$ , respectively. The target was illuminated in transmission with an array of LEDs with a peak wavelength of 515 nm filtered to a bandwidth of 18 nm. This spectral band encompasses the emission peak of proflavine. The prototype objective imaged the resolution target to the proximal end of the coherent fiber bundle, which was placed in the image plane of the objective. A conventional microscope objective (Nikon, 10 $\times$ , 0.3 NA) and a tube lens were used to relay the image of the distal end of the fiber bundle to a digital camera (SenTech STC-TB202USB-AS, 4.4  $\mu\text{m}$  square pixel). Images of the target using only the conventional microscope objective were also taken by removing the fiber bundle and repositioning the relay optics and camera. The target was imaged in air, which slightly reduced the NA and changed the image-plane location, although as the qualitative results in Section 7.2 show, the performance of the objective remained diffraction limited.

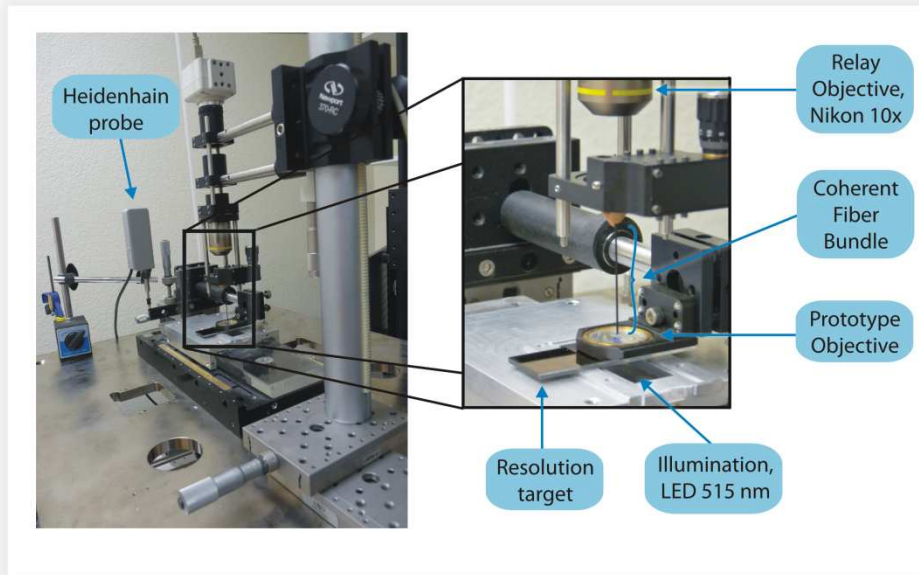


Fig. 10. Photograph of the test set-up for the prototype ultra-slim objective with an enlargement illustrating the key portion of the set-up.

An example of the qualitative imaging performance can be seen in Fig. 11. The image of the target using only the ultra-slim objective is shown in Fig. 11(a). As annotated, the line features in the upper right have a line width of 1  $\mu\text{m}$ . The image in Fig. 11(b) shows the image of the target relayed through the coherent fiber bundle. With the coherent fiber bundle, the achievable resolution is estimated at 2.5  $\mu\text{m}$ . That resolution result compares favorably

with the approximately 4.4  $\mu\text{m}$  resolution reported for using a bare fiber bundle in contact with tissue [3].

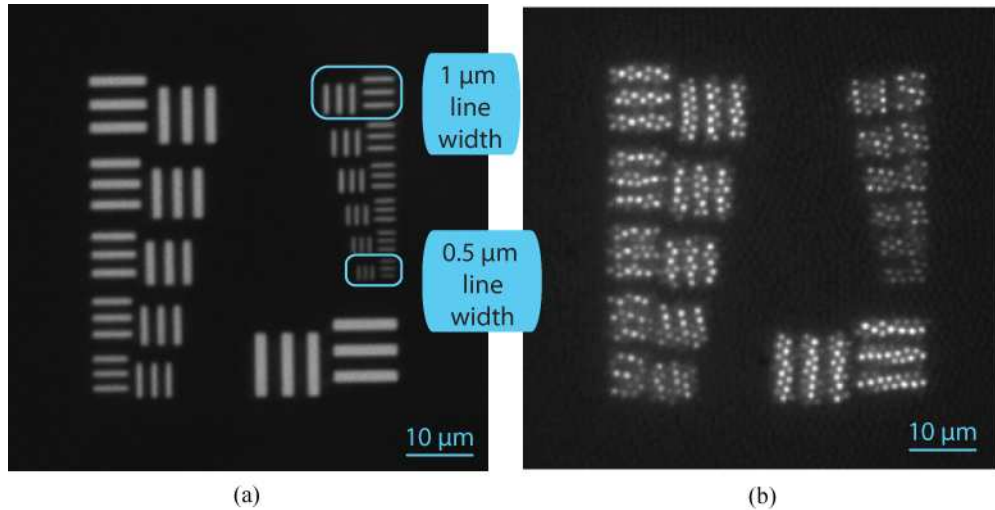


Fig. 11. Imaging results obtained from a custom, miniature US Air Force resolution target. (a) Image obtained directly with the ultra-slim objective, (b) Image obtained through a coherent fiber bundle. See text for details.

### 7.2 Quantitative imaging performance

In order to quantitatively test the image performance of the ultra-slim objective, an image of the grating shown in Fig. 12 was acquired, and two methods were used to estimate the experimental PSF, MTF, and Strehl ratio.

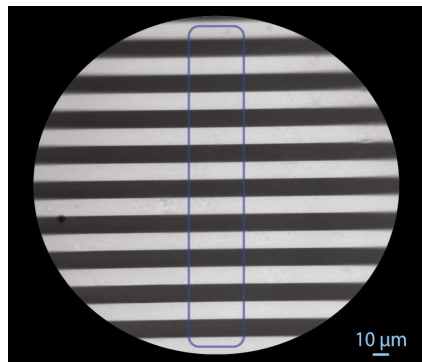


Fig. 12. Grating with 25  $\mu\text{m}$  period used for evaluating the quantitative performance of the objective. The annotated area represents the section over which the Strehl ratio was evaluated at each edge in the image.

The first method is known as the tilted-edge method [16,23,24]. A general diagram of the process can be found in Fig. 13. The first step is to select a section of the image containing a tilted edge as shown in Fig. 13, Step 1. Then the vertical cross-sections of the image are shifted so that the tilt is removed and the edge is aligned as shown Step 2. A curve is fit to the data, resulting in the edge spread function (ESF) shown as the red curve in Step 2. The derivative of the ESF was taken to find the line spread function (LSF) which is also a cross section of the PSF. The cross-section is vertical in this case, i.e., perpendicular to the edge. In the fourth step the Fourier transform of the LSF is taken to find the optical transfer function (OTF), whose modulus produces the MTF [25].

The second method is similar to the tilted-edge method in principle but simpler. The difference is that the second method does not shift the vertical slices of the selected section of data or fit a curve to the edge data as in Step 2 of the tilted-edge method. Instead, the second method averages the slices in the vertical direction of the figure of Step 2 and takes the derivative of the averaged data to find the LSF.

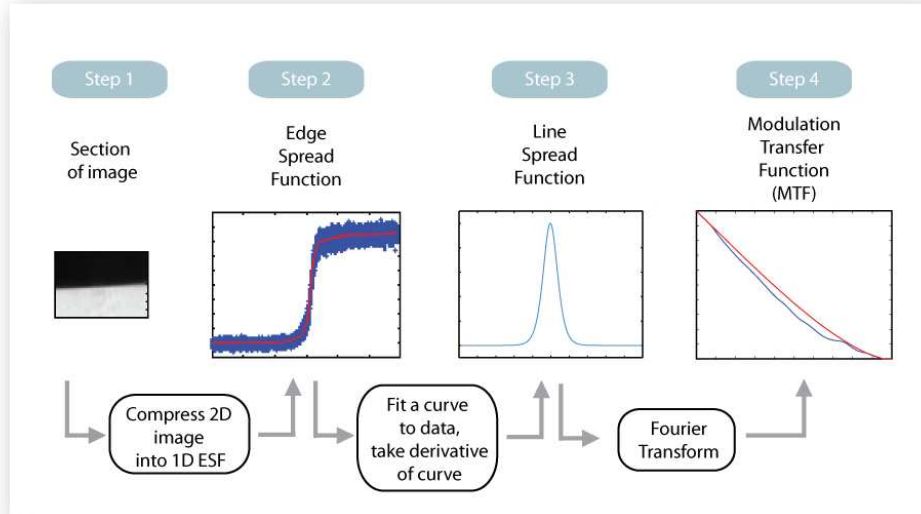


Fig. 13. Map of the tilted edge method for estimating quantitative image performance metrics, such as PSF, MTF and Strehl ratio.

The experimental LSF/PSF data can be found in Fig. 14(a) along with the predicted PSF produced by ZEMAX. Both of the two quantitative methods lead to estimates of the experimental PSF data that closely match the predicted PSF data. The experimental PSF FWHM differs from the predicted PSF FWHM by  $0.25 \mu\text{m}$  [see Table 6]. Figure 14(b) compares the experimental MTF and the predicted MTF.

Additionally, the tilted-edge method results lead to an estimate of the Strehl ratio of greater than 0.8. Both the PSF and MTF, along with the Strehl ratio, confirm that the prototype ultra-slim objective optical system is nearly diffraction limited [19].

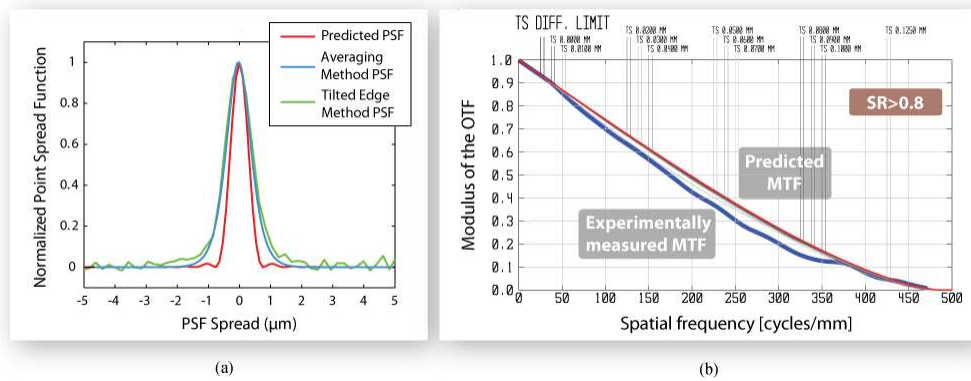


Fig. 14. (a) Plots of the predicted PSF at the object surface as well as the results of two methods of estimating experimental PSF at the object surface, (b) Plot of the predicted, theoretical MTF and the experimentally measured MTF. The MTF curves plotted in this figure refer to the image plane of the ultra-slim objective.

**Table 6. Predicted and Experimental FWHM of PSF**

Method	FWHM ( $\mu\text{m}$ )
Predicted from ZEMAX	0.64
Tilted Edge Method	0.83
Averaging Method	0.89

The lateral resolution was estimated by using the experimental PSF data shown in Fig. 14(a). First, two sets of PSF data were used, one centered at  $0 \mu\text{m}$  and the other with the peak shifted by  $2 \mu\text{m}$ . As the second peak was shifted towards the first, the two sets of PSF data were added, and the ratio of the local minimum between the peaks and the peak value was recorded with respect to the PSF peak separation. The Rayleigh criterion [26], which states that the two points are just resolvable if the ratio of the local minimum and maximum is  $8/\pi^2$ . The lateral resolution was determined as the peak separation that matches the criterion. The lateral resolution of the ultra-slim objective was found to be  $0.9 \mu\text{m}$  by this method.

Additionally, the Strehl ratio was measured across the field at each of the edges in the region shown in Fig. 12. The Strehl ratio varied from 0.45 to greater than 0.8, where a ring with a radius of  $62.5 \mu\text{m}$  and a width of  $55 \mu\text{m}$  had a Strehl ratio larger than 0.8. Also, the circular region with a diameter of  $175 \mu\text{m}$  at the center of the field had a Strehl ratio of 0.7 or higher. The variation in Strehl ratio across the field is a consequence of the curved object surface of our objective and a flat resolution target. The following section reports on the measured field curvature of the fabricated optical system.

### 7.3 Field curvature

The ultra-slim objective was designed purposefully with a small amount of field curvature to help with the lens-design process. Because of the curvature, different annular regions of a flat resolution target come into focus as the system is moved relative to the target. To estimate the sag of the object surface curvature, the mean radius of one of those rings was determined along with the change in the system position relative to the object needed to focus on that annular region. A parabolic model was fitted to the resultant radius and the change in object distance. Lastly, this fit was used to estimate the sag at the  $125\text{-}\mu\text{m}$  edge of the field of view.

To acquire the necessary data, features of the US Air Force resolution target were centered in the FOV as shown in Fig. 15(a). A length gauge (Heidenhain, shown in Fig. 10) was used to monitor the position of the imaging system as a series of images were taken while the

imaging system moved closer to the object. In order to find the in-focus annulus, the modulation of the on-axis features shown as Set 1 in Fig. 15(a) was found by taking the cross-section as shown in Fig. 15(b). The modulation was calculated using

$$\text{Modulation} = \frac{I_{\max} - I_{\min}}{I_{\max} + I_{\min}}. \quad (1)$$

These modulations were compared with the modulation of the corresponding group and element numbers for Set 2 in the series of images to determine which annulus in Set 2 was in best focus.

For this experiment the first element in the right column had the closest modulation between the on-axis Set 1 and the first element in Set 2 when the system had been moved 6  $\mu\text{m}$ . Using the distance between the two feature sets in Fig. 15(a) as the radius of the annulus and the change in the system vertical position, a parabolic fit was performed. The experimental sag across the 250- $\mu\text{m}$  diameter field was estimated using the fit to be 8.5  $\mu\text{m}$ , in good agreement with the design sag of 9.7  $\mu\text{m}$ .

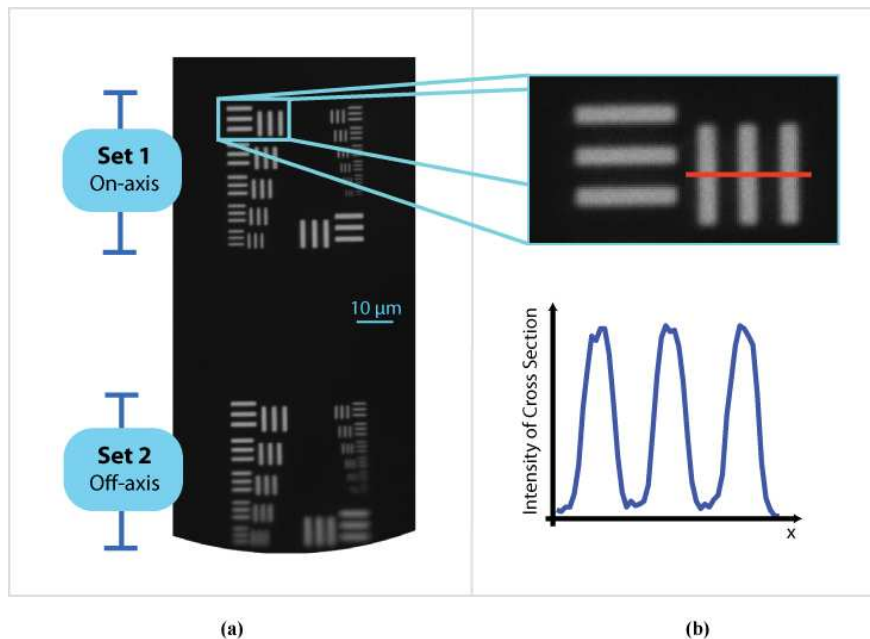


Fig. 15. Illustration of the process for estimating the curvature of the object surface. Part (a) Portion of an acquired image showing a set of on- and off-axis features, Part (b) The modulation of the vertical bars.

## 7. Conclusion

We have presented a design for an ultra-slim, 0.8-mm clear aperture diameter microendoscope objective that balances the tradeoffs of conventional imaging to produce an optical-biopsy system intended for real-time, *in-vivo* imaging for diagnosis of breast cancer. This design builds on the experience gained from previous systems which our group has designed [9,16,27] and is the most compact form yet in order to match the requirements of optical biopsy. In particular, the OD was reduced while maintaining a NA that results in a spatial resolution of 0.9  $\mu\text{m}$  and a 250- $\mu\text{m}$  field of view. By characterizing the coherent fiber bundle's light-coupling efficiency, we were able to relax the image-space telecentricity constraint, thereby allowing a further reduction in OD. Lastly, we were able to develop an all-plastic objective design after confirming experimentally the negligible level of autofluorescence of candidate optical-plastic materials. The results of the autofluorescence

study showed that while Zeonex E48R does autofluoresce at the excitation wavelength of 470 nm, the emitted signal from the lenses was significantly less than the signal from the tissue. Additionally, we have shown that the optics for the ultra-slim objective can be made by modern manufacturing processes and achieve diffraction-limited imaging performance. Specifically, the objective exhibits a Strehl ratio of 0.8 and a lateral resolution of 0.9  $\mu\text{m}$  with a designed field of view of 250  $\mu\text{m}$ . The next step in this project will be to fabricate and assemble the ultra-slim objective demonstrated here to its intended diameter of 1 mm.

### **Acknowledgments**

This work was supported by the US National Institutes of Health (NIH) grants R01 EB007594 and R01 CA124319 as well as an IBB Medical Innovation Award from the Richardson Family Foundation to TT and the University of Arizona TRIF Imaging Fellowship Program. The authors thank Dr. Urs Utzinger of the University of Arizona for his assistance with autofluorescence measurements.